

CMB delensing with deep learning

Shulei Ni,^{1,2} Yichao Li¹ and Xin Zhang^{1,3,4}*

¹Key Laboratory of Cosmology and Astrophysics (Liaoning Province) & College of Sciences, Northeastern University, Shenyang 110819, China

²Research Center for Astronomical Computing, Zhejiang Laboratory, Hangzhou 311121, China

³Key Laboratory of Data Analytics and Optimization for Smart Industry (Ministry of Education), Northeastern University, Shenyang 110819, China

⁴National Frontiers Science Center for Industrial Intelligence and Systems Optimization, Northeastern University, Shenyang 110819, China

Accepted XXX. Received YYY; in original form ZZZ

ABSTRACT

The cosmic microwave background (CMB) stands as a pivotal source for studying weak gravitational lensing. While the lensed CMB aids in constraining cosmological parameters, it simultaneously smooths the original CMB’s features. The angular power spectrum of the unlensed CMB showcases sharper acoustic peaks and more pronounced damping tails, enhancing the precision of inferring cosmological parameters that influence these aspects. Although delensing diminishes the B -mode power spectrum, it facilitates the pursuit of primordial gravitational waves and enables a lower variance reconstruction of lensing and additional sources of secondary CMB anisotropies. In this work, we explore the potential of deep learning techniques, specifically the U-Net++ algorithm, to play a pivotal role in CMB delensing. We analyze three fields, namely T , Q , and U sky maps, present the angular power spectra of the CMB delensed TT , EE , BB , and TE , and compare them with the unlensed CMB angular power spectra. Our findings reveal that the angular power spectrum of the lensed CMB, processed by U-Net++, closely aligns with that of the unlensed CMB. Thus, U-Net++ based CMB delensing proves to be effective in mitigating the impacts of weak gravitational lensing, paving the way for enhancing the CMB delensing power spectrum in forthcoming CMB experiments. The code utilized for this analysis is available on [GitHub](#).

Key words: cosmology: cosmic microwave background – cosmology: gravitational lensing

1 INTRODUCTION

The anisotropies of the cosmic microwave background (CMB) offer crucial insights into the early universe. Observations of such anisotropies have made significant contributions to establishing the current standard model of cosmology. In the last few decades, three generations of satellite experiments, namely *COBE* (Smoot et al. 1992; Fixsen et al. 1996; Bennett et al. 1996), *WMAP* (Spergel et al. 2003; Komatsu et al. 2009, 2011), and *Planck* (Ade et al. 2014b, 2016; Aghanim et al. 2020), as well as numerous ground-based experiments (e.g., DASI (Leitch et al. 2002), CBI (Readhead et al. 2004), SPT-pol (Carlstrom et al. 2011), BICEP (Barkats et al. 2014; Ade et al. 2014c), Keck Array (Staniszewski et al. 2012), ACT (Coulton et al. 2023), and Ali-CPT (Li et al. 2019)) and balloon experiments (e.g., BOOMERanG (Masi et al. 2002), EBEX (Aboobaker et al. 2018), SPIDER (Crill et al. 2008)), have been carried out to precisely measure the temperature and polarization power spectrum of the CMB. Moreover, there are several ongoing plans for diverse experimental projects, including *LiteBIRD* (Allys et al. 2023), CMB-S4 (Abazajian et al. 2016, 2022), and PIPER (Lazear et al. 2014), being devoted to the detection of CMB polarization signals.

The generation of the stochastic background of gravitational waves, known as primordial gravitational waves (PGWs), is a fundamental prediction in any cosmological inflation model (Lyth &

Riotto 1999; Baumann 2011). The characteristic of this signal encodes unique information about the physics of the early universe and its subsequent evolution, providing an exciting and powerful window into the universe’s origin and evolution.

The tensor-to-scalar ratio r parameterizes the amplitude of PGWs and connects to the energy scale at which inflation occurred. Therefore, the detection of PGWs is expected to reveal the physical properties of the universe’s early stages. Fortunately, these PGWs have distinct imprints in the polarized anisotropy of the CMB, displaying a spiral-like B -mode pattern that enables the extraction of the PGW signal from the polarized B -mode of the CMB (Ade et al. 2014a; Abazajian et al. 2016). The detection of B -mode signals presents an exceptionally challenging task, particularly due to the uncertain extent of foreground contamination and the mixing of relatively strong E -mode signals with B -mode signals induced by weak gravitational lensing (Ade et al. 2014a). Therefore, the primary scientific objectives of CMB polarization observations currently entail determining the extent of foreground contamination and precisely measuring the effect of gravitational lensing (Ade et al. 2019). Our research primarily centers on the gravitational lensing phenomenon associated with CMB.

CMB lensing has been extensively studied in theory (Lewis & Challinor 2006; Okamoto & Hu 2003; Bartelmann & Schneider 2001). After decoupling from matter at the last scattering surface, CMB photons propagate freely and are gravitationally deflected by the universe’s large scale distribution of matter. The lensing effect

* zhangxin@mail.neu.edu.cn

results in subtle imprints on the CMB temperature and polarization anisotropies. These can be utilized to create a map of the lensing potential that determines the lensing deflections’ gradient (Hu 2000). Weak gravitational lensing smoothes the acoustic peaks of the CMB angular power spectra, transferring power from larger angular scales to smaller scales, and converting E -mode polarization to B -mode polarization (Zaldarriaga & Seljak 1998; Dodelson & Schmidt 2021). In addition, weak gravitational lensing can induce small distortions in the CMB, and these distortions can be detected by modifying its primordial morphology in an anisotropic form.

Given that the anisotropy during the final scattering can be approximated as Gaussian, the non-Gaussian structures observed in the lensed CMB sky provide additional information about the properties of gravitational lensing material. This is crucial for a further understanding of important details regarding the distribution of matter (Lewis et al. 2000; Lewis & Challinor 2006; Lewis 2013). Therefore, weak gravitational lensing of the CMB both promotes and hinders our comprehension of the history and content of the universe.

There are several advantages associated with mitigating the impacts of lensing on the observed CMB temperature and polarization maps (Lewis 2005; Lewis & Challinor 2006; Lewis 2013; Dodelson & Schmidt 2021). Firstly, the average temperature of the CMB remains unchanged by lensing as the gravitational effect only adjusts arrival directions and not the surface brightness (Lewis 2005, 2013). Secondly, the distortion of light paths traveling from far sources to reach us is caused by the gravitational effect of universe’s inhomogeneities. The reason lensing is so promising is that it enables probing all clustering stress-energy components in the universe through spacetime perturbations since light paths react to mass. Measurement of these distortions provides insight into the mass distribution of the universe (Lewis 2005; Lewis & Challinor 2006; Lewis 2013).

However, gravitational lensing has the potential to smoothen acoustic peaks in the CMB. This can be comprehended by considering that when photons get deflected, features of a fixed angular size can either be magnified or de-magnified, causing sharp features in the power spectrum to be blurred across a range of scales. The angular scale of sharp features in the power spectrum is easier to measure than broad humps; consequently, gravitational lensing weakens our ability to precisely measure acoustic peak positions in the CMB power spectra (Lewis 2005; Lewis & Challinor 2006). The temperature power spectrum undergoes lensing by 0.2% at $\ell \sim 2000$, but smaller scales experience changes at the percentage level. The impact on the B -mode polarization power spectrum is more significant, with power increase of 6% across all scales (Lewis & Challinor 2006).

Delensing reverses this peak smoothing, providing sharper peaks with a more precisely measurable angular scale. Similar observations can be made about the measurement of peak heights. Weak gravitational lensing alters the CMB power spectra, induces non-Gaussian, and generates a B -mode polarization signal, which causes confusion for the signal from PGWs (Lewis 2005; Lewis & Challinor 2006).

In recent years, deep learning and artificial intelligence techniques have developed rapidly, gaining widespread attention and significant application in various disciplines. Astronomy research has been catching up, and many studies have emerged, applying deep learning for data analysis (Gupta et al. 2018; Caldeira et al. 2019; Zhou et al. 2018; Zhang et al. 2019; Zhou et al. 2019; Springer et al. 2020; Mäkinen et al. 2021; Guzman & Meyers 2022; Ni et al. 2022; Gao et al. 2023). These studies have demonstrated the high effectiveness of deep learning in image reconstruction and segmentation tasks, enabling the detection of features at the pixel level (Wang et al. 2018; Ghosh et al. 2019; Minaee et al. 2021).

This work adopts the sky map segmentation method proposed by Mäkinen et al. (2021). The method relies on the Healpix pixelization scheme, which divides the two-dimensional spherical sky map into multiple two-dimensional plane images. We apply this sky map segmentation method to attempt a novel CMB delensing approach that can remove the lensing effect.

The paper is organized as follows. In Section 2, we present a fundamental overview of CMB and lensing, along with a clear problem statement. This section also encompasses simulations of both CMB lensing and unlensing data, as well as noise simulation. Section 3 delves into the details of the U-Net++ architecture, data pre-processing techniques, and the predictions generated by U-Net++. In Section 4, we provide a comprehensive analysis of the obtained results. Finally, Section 5 provides the concluding remarks.

2 DATA SIMULATION

In this section, we will provide a comprehensive description of the simulated CMB and noisy sky maps used in our analysis. This includes detailed information on both the lensed temperature and polarization maps with noise, as well as the unlensed temperature and polarization maps.

For our simulations, we employed the publicly available package (*Lenspyx*¹) (Lewis 2005; Diego-Palazuelos et al. 2020), a Python package specifically designed for simulating lensed CMB maps on a curved sky. We also relied on three additional software packages, namely *CAMB*² (Lewis et al. 2000), *LensPix*³ (Lewis 2005) and *Healpy*⁴ (Górski et al. 2005; Zonca et al. 2019), as the foundational components for developing detailed curved-full-sky simulations of both lensed and unlensed CMB. By incorporating the *Planck* 2018 CMB lensing pipeline (*plancklens*), *Lenspyx* has the ability to replicate both the published map and band-powers.

We have employed a concise formula to generally describe our data simulation process, which is presented as follows:

$$\mathcal{M}_{\text{lensed}}^{\mathcal{F}} = \text{Smooth}[\text{Lenspyx}(\mathcal{M}_{\text{unlensed}}^{\mathcal{F}}) + \mathcal{M}_N^{\mathcal{F}}], \quad (1)$$

where, \mathcal{M} represents the full sky map, and $\mathcal{F} \in \{T, Q, U\}$. *Smooth* represents the telescope’s beam, and we have chosen a simple Gaussian beam. *Lenspyx* is an abbreviation for the process of converting unlensed maps into lensed maps. N represents the noise component in the image. Here, *Smooth* and *Lenspyx* can be regarded as operators, corresponding to the operations of achieving smoothing and lensing, respectively.

During the simulation process, we employed the *HEALPix* pixelization strategy. Given the significant importance of small-scale analysis, we deliberately selected a sky map with a resolution of $N_{\text{side}} = 2048$, corresponding to an angular resolution of 1.718 arcminutes.

We have considered the simple instrumental effect, namely the influence of the Gaussian beam. In order to more accurately simulate the observational data, we adopt the full width at half maximum (FWHM) from existing full sky observation experiments in subsequent simulations to convolve the sky map.

¹ <https://github.com/carronj/lenspyx>

² <https://camb.info/>

³ <https://cosmologist.info/lenspix/>

⁴ <https://github.com/healpy/healpy/>

Table 1. Instrument and noise specifications used to produce the simulations in this work. In the table, θ_{FWHM} represents the telescope’s full width at half maximum; $\text{NET}(T/P)$ denotes the effective temperature of the instrument, with T referring to the temperature field and P indicating the polarization field; N_{det} stands for the number of detectors; ΔT signifies the total observation time; f_{sky} represents the fraction of the sky observed within the ΔT timeframe; and Y assumes a value of 1 under ideal conditions.

θ_{FWHM} [arcmin]	$\text{NET}(T/P)$ [$\mu\text{K}\sqrt{\text{sec}}$]	N_{det} [count]	f_{sky} [%]	Y [Yield]	ΔT [sec]
10.7	38/2.1	1020	80	1	1.5×10^5

2.1 Noise simulation

In the course of the actual observation of the CMB, it is crucial to consider various sources of noise interference. Given the faintness of the CMB signal, noise has the potential to mask or distort its true characteristics, leading to deviations in the measurement of core observables such as temperature and polarization. Moreover, the presence of noise can introduce systematic errors that impact our ability to infer cosmological parameters.

The noise in CMB detectors is often approximated as Gaussian white noise, and its angular power spectral density can be defined in the following (Hanany et al. 2019; Diego-Palazuelos et al. 2020; Wolz et al. 2023):

$$N_{\ell}^{XX'} = [s^2 e^{(-\ell(\ell+1) \frac{\theta_{\text{FWHM}}^2}{8 \ln 2})}]^{-1}, \quad (2)$$

where $X \in \{T, E, B\}$, θ_{FWHM} stands for the FWHM of the telescope, which is related to the observation frequency. Additionally, s denotes the telescope’s sensitivity, which is defined as (Wu et al. 2014; Ade et al. 2015; Wu et al. 2020)

$$s^{-1} [\mu\text{K rad}] = \frac{\text{NET} [\mu\text{K} \sqrt{\text{sec}}] \sqrt{4\pi f_{\text{sky}} [\text{rad}^2]}}{\sqrt{N_{\text{det}} Y \Delta T [\text{sec}]}} \quad (3)$$

where NET represents the instrument equivalent temperature, N_{det} is the number of detectors, f_{sky} denotes the observed sky fraction, and we assume an ideal case where yield $Y = 1$, and ΔT represents the observation duration.

Our research primarily aims to comprehensively examine the potential of delensing rather than extensively investigate the specific impact of noise in the delensing process. To fulfill this research objective, we have intentionally selected a specific frequency, namely 75 GHz (Akrami et al. 2020; Hanany et al. 2019; Allys et al. 2023), as the sole focus of our in-depth analysis. Furthermore, considering that our analysis relies on full-sky data, we employed the instrument parameters of PICO (Hanany et al. 2019), the next-generation space telescope, to simulate the noise, as detailed in Table 1.

After substituting the parameters into Equations (2) and (3), we can calculate the temperature and polarization angular power spectra of noise, as illustrated in Figures 1 and 2. For the noise of each component, we generate corresponding full sky maps based on their angular power spectra and stack these maps onto the sky maps with lensing effects. Through this process, we obtain the training dataset required for the U-Net++ model in subsequent studies.

2.2 The CMB temperature and lensing potential

The CMB radiation field is represented by the temperature anisotropy, denoted as $T(\hat{n})$, and the polarization, denoted as $P(\hat{n})$, in the spatial direction \hat{n} of the celestial sphere. We observe CMB temperature changes projected on a 2D spherical surface sky, and it is now habit-

ual in the literature to expand the temperature field using spherical harmonics.

The temperature fluctuation of the CMB on the spherical surface is described by a scalar field, consisting of small fluctuations $\Delta T(\hat{n})$ at a level of 10^{-5} relative to the average value $T_0 = 2.725$ K. For full-sky observations, the temperature field T can be expressed through the spherical harmonic decomposition using spin-0 spherical harmonics $Y_{\ell m}(\hat{n})$,

$$\Delta T(\hat{n}) = \sum_{\ell=0}^{\ell_{\text{max}}} \sum_{m=-\ell}^{m=\ell} a_{\ell m} Y_{\ell m}(\hat{n}). \quad (4)$$

All the information contained in the temperature field $T(\hat{n})$ is included in the space-time dependent amplitudes $a_{\ell m}$, where $a_{\ell m}$ represents the spherical harmonic coefficient and can be expressed using the following formula,

$$a_{\ell m} = \int d\Omega_{\hat{n}} \Delta T(\hat{n}) Y_{\ell m}^*(\hat{n}), \quad (5)$$

and analogously to the methodology in Fourier space, we can define an angular power spectrum for these fluctuations, denoted as C_{ℓ} , by calculating the variance of the harmonic coefficients,

$$\langle a_{\ell m} a_{\ell' m'}^* \rangle = \delta_{\ell \ell'} \delta_{m m'} C_{\ell}, \quad (6)$$

where the above average is taken over many ensembles and the delta functions arise from isotropy. We can write the following expression for the angular power spectrum,

$$C_{\ell}^{TT} = \frac{1}{2\ell + 1} \sum_m \langle a_{\ell m}^T a_{\ell m}^{T*} \rangle. \quad (7)$$

We can simulate the angular power spectrum C_{ℓ} with CAMB or CLASS⁵ (Lucca et al. 2020; Di Dio et al. 2013), as shown in Fig. 1. The figure demonstrates that as the scale decreases, the difference between lensed and unlensed data amplifies. This phenomenon occurs due to the deflection imparted on CMB photons by each encountered potential, resulting in an accumulation of effects on the CMB power spectrum at small scales. Consequently, the lensing effect distorts the original power spectrum and introduces non-Gaussianity in the lensed CMB (Lewis & Challinor 2006). It should be noted that non-linear evolution also contributes to an increase in power on smaller scales.

Weak lensing of the CMB deflects photons coming from an original direction \hat{n}' on the last scattering surface to direction \hat{n} on the observed sky, so a lensed CMB temperature field, $T(\theta, \phi)$, is given by $\tilde{X}(\hat{n}) = X(\hat{n}')$ in terms of the unlensed field $X = T$ (Lewis 2005). Thus the position in the sky where we finally see the CMB photons is determined by the integral of the gravitational potential along the line of sight to the last scattering surface.

We propose the definition of an integrated lensing potential, denoted as ψ . The deflection vector is expressed as the gradient of the lensing potential, $\nabla\psi(\hat{n})$, where ∇ represents the covariant derivative on the sphere. The vector \hat{n}' is derived from \hat{n} by moving its geodesic at one end of the surface of the unit sphere along the \hat{n}' direction by a distance $\nabla\psi(\hat{n})$. Then the unlensed CMB photon with direction \hat{n} becomes a lensed CMB photon with direction $\hat{n} = \hat{n}' + \nabla\psi(\hat{n})$, through the weak gravitational lensing. Thus, the lensed CMB temperature can be written as follows,

$$\tilde{T}(\hat{n}) = T(\hat{n}') = T(\hat{n} + \nabla\psi(\hat{n})), \quad (8)$$

⁵ https://lesgourg.github.io/class_public/class.html

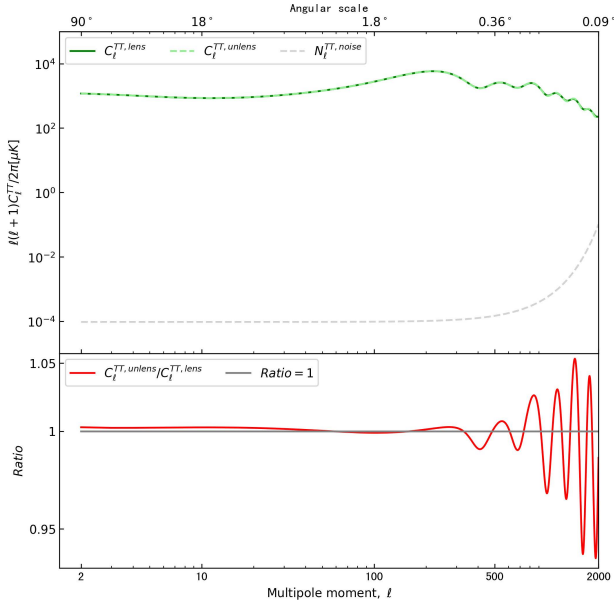


Figure 1. Effect of lensing on the CMB temperature power spectrum. *Top panel:* The solid green line represents the unlensed CMB TT angular power spectrum. The light green dashed line represents the lensed CMB TT angular power spectrum. The gray dashed line depicts the contribution of noise to the TT angular power spectrum. *Bottom panel:* The fractional difference between these very similar spectra. The red solid line illustrates the ratio between the unlensed TT spectrum and the lensed TT spectrum, while the gray solid line represents the reference line where the ratio equals 1.

where lensing potential $\psi(\hat{n})$ can be defined as (Lewis & Challinor 2006; Hassani et al. 2016),

$$\psi(\hat{n}) = 2 \int_0^{\chi^*} d\chi \left(\frac{\chi^* - \chi}{\chi^* \chi} \right) \Psi(\hat{n}, \eta), \quad (9)$$

where η is the conformal time, χ is the comoving distance and Ψ is the Bardeen potential. As with the CMB temperature angular power spectrum, the same angular power spectrum of the gravitational potential can be obtained,

$$C_\ell^{\psi\psi} = 16\pi \int \frac{dk}{k} P_R(k) \left(\int_0^{\chi^*} d\chi \left(\frac{\chi^* - \chi}{\chi^* \chi} \right) T(k, \eta) k_\ell(k\chi) \right)^2, \quad (10)$$

where $T(k, \eta)$ is the appropriate transfer function, $P_R(k)$ is the primordial power spectrum. We will employ either CAMB or CLASS to simulate the power spectrum of the lensing potential.

The CMB photons are deflected by the gravitational lensing effect of massive cosmic structures as they travel across the universe. Researchers have been able to measure this gravitational lensing of the CMB across the full sky using data from CMB satellites. Figure 1 shows the lensed TT angular power spectrum and the unlensed TT power spectrum, along with their ratios. On large scale, the anisotropies of the CMB are primarily dominated by emissions from the last scattering surface at a redshift of $z \sim 1100$. However, on smaller scale, the CMB is more significantly influenced by what are known as secondary effects. These secondary anisotropies arise as a result of interactions between CMB photons and matter along the line of sight. Consequently, as seen in the bottom panel of Figure 1, the small-scale angular power spectrum is more significantly affected by the lensing potential.

We utilized `Lenspyx` to simulate lensed CMB and unlensed CMB temperature and polarization sky maps. In our simulation, we uti-

lized the best-fit cosmological parameters from the *Planck* 2018 Λ CDM results (Aghanim et al. 2020), i.e., $H_0 = 67.7 \text{ km s}^{-1} \text{ Mpc}^{-1}$, $\Omega_b = 0.049$, $\Omega_m = 0.311$, $\Omega_\Lambda = 0.689$, and $\sigma_8 = 0.81$. For the simulation of the temperature sky map, we ran the parameters A_s and n_s , as they are more sensitive to it, while for the polarization, we only concentrate on the tensor-to-scalar ratio. Both temperature and polarization simulations were conducted autonomously.

To acquire additional datasets and account for the interdependence of deep learning models, we conducted experiments using two key parameters: the power spectrum amplitude (A_s) and spectral index (n_s) for CMB temperature power spectra and sky maps. Specifically, we tested 5 values of A_s (2.2×10^{-9} , 2.3×10^{-9} , 2.4×10^{-9} , 2.5×10^{-9} , 2.6×10^{-9}) and 3 values of n_s (0.986, 0.996, 1.06). To address the effects of lensing potential on small scales, a high-resolution simulation with $N_{side} = 2048$ was utilized. In order to ensure a closer alignment between the simulation results and actual observations, we considered the smoothing effect of the telescope beam on the signal. During the computational phase, we opted for the Gaussian beam as an approximate model for beam shaping to streamline the process.

Figure 4 illustrates the comparison of differences between the CMB T , Q , U sky maps affected by lensing effects and those unaffected by lensing effects. The inputted final dataset for training the U-Net++ model will undergo the influence of the telescope beam effect, which will be manifested as a smoothing effect due to a Gaussian beam with a σ value of 0.00311 rad. Conversely, the corresponding label data will remain unaltered without any modifications.

2.3 The CMB polarization

CMB polarization is measured through time-averaged Stokes parameters – measures of linear polarization of the electric field aligned orthogonally to the line of sight’s (LOS) Cartesian axes. Due to the nature of Thomson scattering, Q and U are ample in describing CMB polarization, given their inability to generate circular polarization (Dodelson & Schmidt 2021). Astronomical observations reveal that Stoke parameters Q and U are linked by a constant and relative 45° degree rotation around LOS – whereas the reference frame may revolve freely around it. Bundling the reference frame with a fixed set of normal vectors in rotation will directly link Q and U to the E and B modes.

In this subsection, we provide a concise overview of the polarization field properties and its decomposition into physically distinct E and B modes. We express the standard construction of E and B fields in terms of the spin-raising and spin-lowering operators, usually implemented in harmonic space.

If we rotate Q and U by an angle α on the plane that is perpendicular to the direction of \hat{n} , we obtain the following solution (Zaldarriaga & Seljak 1997; Zaldarriaga 1998; Rotti & Huffenberger 2019),

$$(Q \pm iU)'(\hat{n}) = e^{\mp 2i\alpha} (Q \pm iU)(\hat{n}). \quad (11)$$

We can derive the separation of E and B modes from the Stokes parameters (Kamionkowski et al. 1997a,b; Bunn et al. 2003; Kamionkowski & Kovetz 2016; Kim & Naselsky 2010). Here we provide a brief overview of the standard method. Additionally, we can decompose Q and U into ± 2 spin spherical harmonics concerning rotation as shown below (Zaldarriaga & Seljak 1997; Zaldarriaga 1998),

$$Q(\hat{n}) \pm iU(\hat{n}) = \sum_{\ell, m} a_{\pm 2, \ell m \pm 2} Y_{\ell m}(\hat{n}), \quad (12)$$

where $_{\pm 2} Y_{\ell m}(\hat{n})$ are the spin ± 2 spherical harmonics, and the coef-

ficients $a_{\pm 2, \ell m}$ are given by

$$a_{\pm 2, \ell m} = \int (Q(\hat{n}) \pm iU(\hat{n}))_{\pm 2} Y_{\ell m}^*(\hat{n}) d\hat{n}. \quad (13)$$

The E and B modes in the spherical harmonic space are formed by

$$\begin{aligned} a_{\ell m}^E &= -(a_{2, \ell m} + a_{-2, \ell m})/2, \\ a_{\ell m}^B &= -(a_{2, \ell m} - a_{-2, \ell m})/2i. \end{aligned} \quad (14)$$

By applying the angular correlation function, the sum can be reduced to an expression that only involves ℓ and power spectrum term

$$\begin{aligned} C_{\ell}^{TE} &= \frac{1}{2\ell+1} \sum_m \langle a_{\ell m}^T a_{\ell m}^{E*} \rangle, \\ C_{\ell}^{EE} &= \frac{1}{2\ell+1} \sum_m \langle a_{\ell m}^E a_{\ell m}^{E*} \rangle, \\ C_{\ell}^{BB} &= \frac{1}{2\ell+1} \sum_m \langle a_{\ell m}^B a_{\ell m}^{B*} \rangle. \end{aligned} \quad (15)$$

Based on the theoretical derivation mentioned above, we adopted the same method for simulating temperature sky maps and tested 15 datasets using two critical parameters, the equation-of-state parameter of dark energy w ($-1.025, -1, -0.975$) and tensor-to-scalar ratio r ($0.001, 0.002, 0.003, 0.004, 0.005, 0.006, 0.007, 0.008, 0.009, 0.01$). As a result, we obtained the sky maps of Q -mode and U -mode in real space and showed the difference between the unlensed and lensed sky maps as shown in Figure 4. Similar to the treatment of the temperature field T , Gaussian beam smoothing was also applied to Q and U using a σ value of 0.00311. Following this step, we obtained the training dataset for Q and U , with the important caveat that their respective labels remain as unlensed signals.

3 U-NET++ STRUCTURE AND DATA PRE-PROCESSING

This section introduces the deep neural network architecture U-Net++ (Zhou et al. 2018, 2019) employed in our CMB delensing analysis. In this paper, we utilize the derivative network of U-Net++, called U-Net 2+, as shown in Figure 5. U-Net++ is an enhanced version of the U-Net architecture, incorporating an improved architecture to facilitate the fusion of multiscale features efficiently. The U-Net network is a type of convolutional neural network (CNN) that was initially designed for biomedical image segmentation (Ronneberger et al. 2015). However, it includes considerable structural modifications based on the CNN. The primary objective is to incorporate a sequence of layers to the standard contracting network, with an upsampling operation instead of the pooling operation. As a result, the resolution of the output is increased. The expanded path is relatively symmetrical with the contracted half, generating a U-shaped structure (Ronneberger et al. 2015).

Specifically, the left side of the U-Net is the downsampling (encoder) part, which is used to extract abstract features from the image. By using convolution and downsampling operations, the image size is reduced to extract shallow features. The convolution operation uses valid padding method, ensuring that the results are based on the context features without missing information. Therefore, after each convolution, the size of the image will be reduced.

In essence, the task of semantic segmentation entails distinguishing a particular class of images from other image classes through the utilization of segmentation masks. It can also be considered as image classification at a pixel level. Our work aims to classify the sky map of CMB temperature via convolution and convolution with the ultimate purpose of delensing CMB. As a result, our network also involves regression operations.

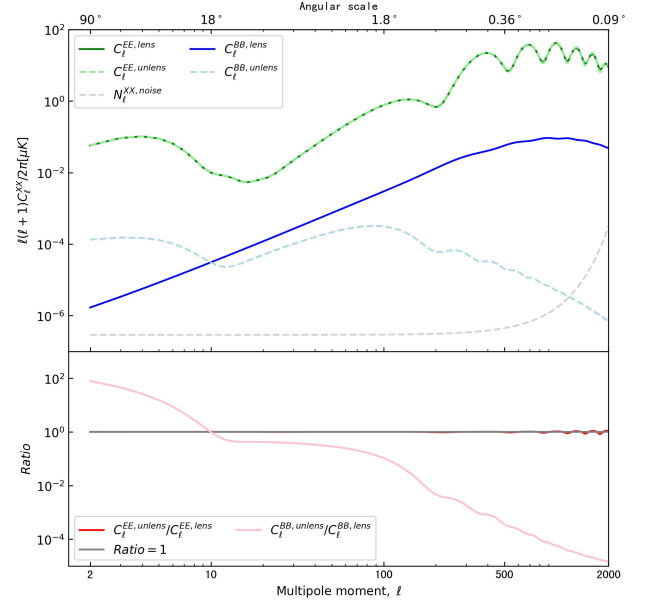


Figure 2. CMB XX angular power spectrum, $X \in \{E, B\}$. *Top panel:* The green solid line represents the lensed EE spectrum, while the light green dashed line denotes the unlensed EE spectrum. The blue solid line indicates the lensed BB spectrum, and the light blue dashed line represents the unlensed BB spectrum. The gray solid line depicts the polarization spectrum, encompassing both the EE spectrum and BB spectrum. *Bottom panel:* The fractional difference between these very similar spectra. The red solid line illustrates the ratio between the unlensed EE spectrum and the lensed EE spectrum, while the pink solid line represents the ratio between the unlensed BB spectrum and the lensed BB spectrum, while the gray solid line represents the reference line where the ratio equals 1.

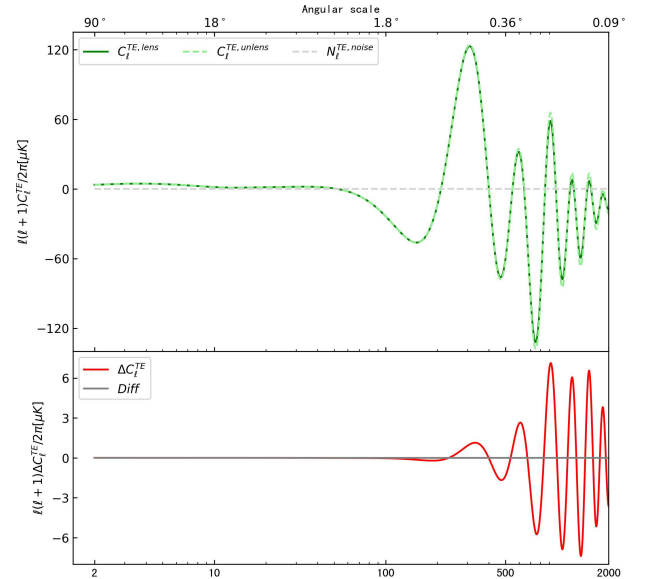


Figure 3. The impact of lensing on the CMB TE power spectrum. *Top panel:* The solid green line depicts the CMB TE angular power spectrum in the absence of lensing. The light green dashed line represents the CMB TE angular power spectrum including the effects of lensing. The gray dashed line illustrates the contribution of noise to the TE angular power spectrum. *Bottom panel:* The difference between these closely related spectra is shown. The red solid line represents the difference between the TE spectrum without lensing and with lensing, and the gray solid line, as a reference line, represents the position where the difference is equal to 0.

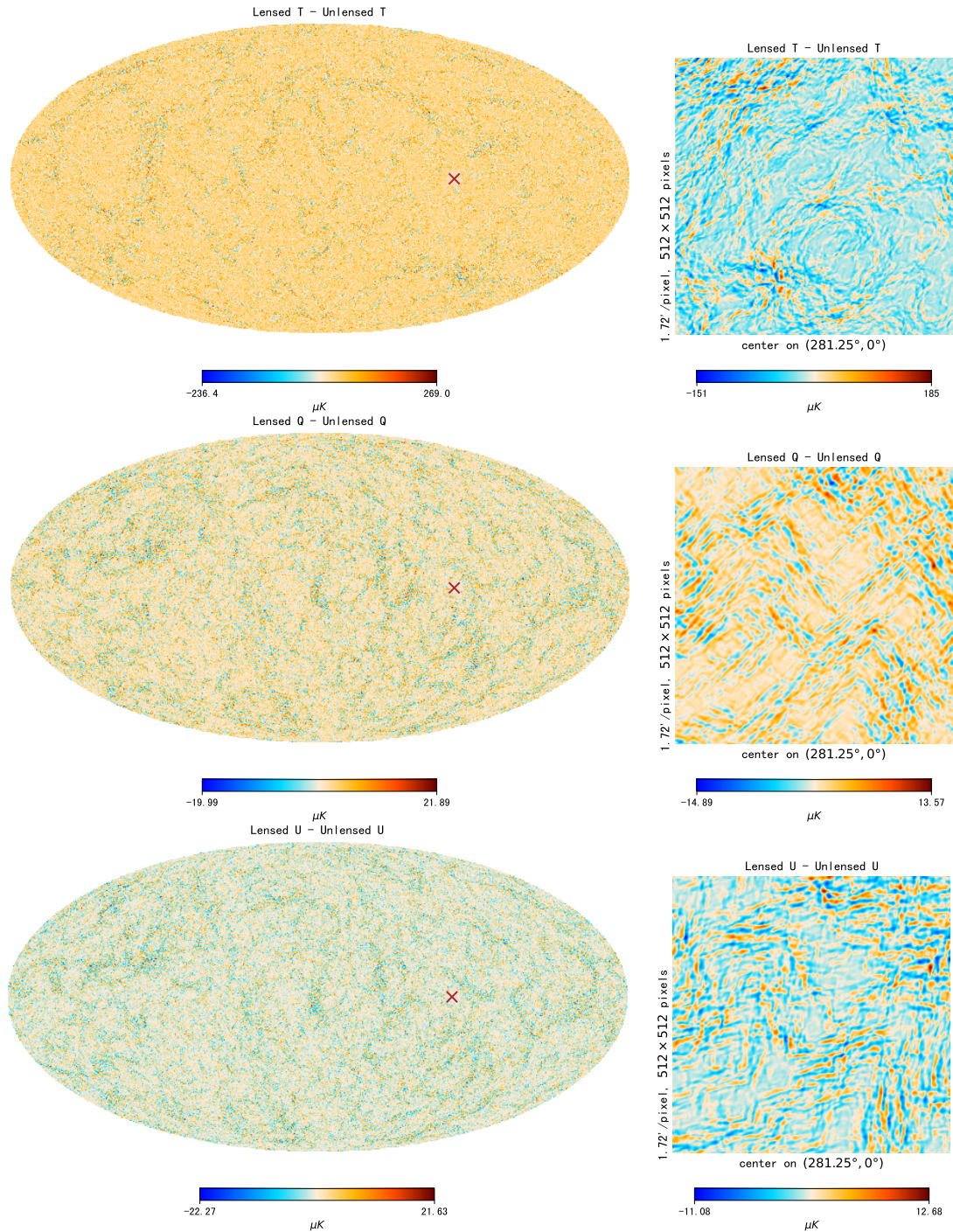


Figure 4. The comparison between the lensed and unlensed CMB maps. The left panel showcases the temperature (T) and polarization (Q , U) differences on a full sky map with a resolution of $N_{side} = 2048$. The map is presented in galactic coordinates, and the units of maps is μK . On the other hand, the right panel illustrates a patch sky map that focuses on a specific region. This patch map has a size of 512×512 , and its center is located approximately at (281.25, 0) on the left panel. The pixel resolution of the patch map is approximately 1.72 square arcminutes.

3.1 U-Net++ structure

U-Net++ is a versatile image segmentation architecture developed to enhance image segmentation accuracy. It comprises U-Net++ networks of various depths, with decoders interconnected at the same resolution by means of an improved skip route. By incorporating dense blocks and convolutional layers between the encoder and de-

coder, it boosts image segmentation accuracy. U-Net++ can be pruned at inference time, if trained with deep supervision, i.e., choose a different output.

Figure 5 shows a unified U-Net++ architecture that merges four U-Nets of varying depths. These U-Nets generate four outputs, designated output 1-4. In the graphical abstract, the original U-Net appears as yellow, with skip connections depicted by dot arrows, and the four

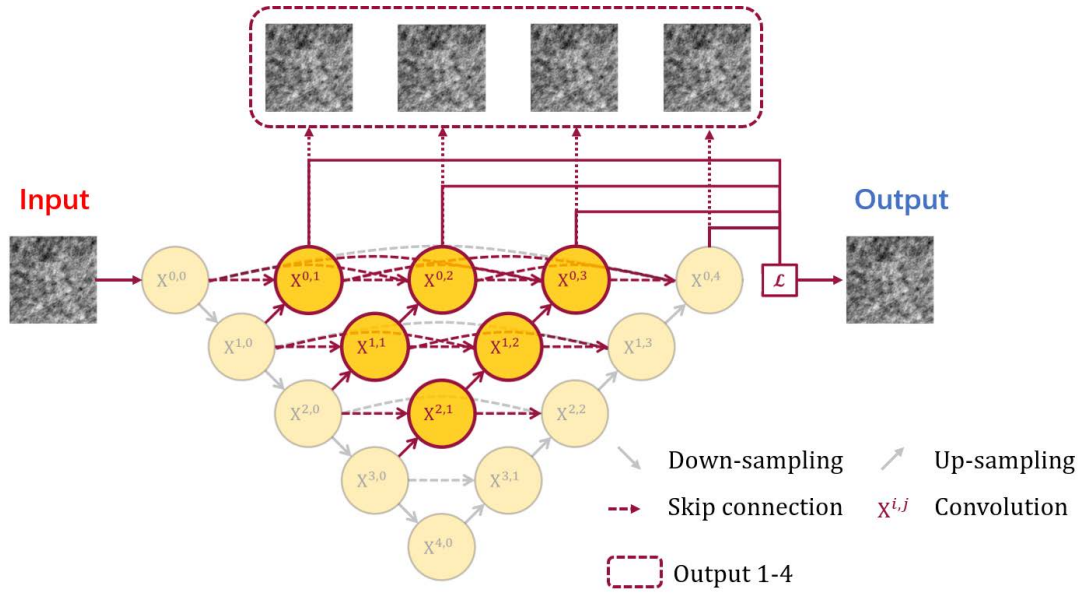


Figure 5. Evolution from U-Net to U-Net++. Each node in the graph represents a convolution block, downward arrows indicate down-sampling, upward arrows indicate up-sampling, dot arrows indicate skip connections, and the dot box indicates the four outputs. U-Net++ combines U-Nets of different depths into a unified architecture. All substructures share the same encoder, but have their own decoders. Then skip connections are dropped, and every two neighboring nodes are connected with a short skip connection, enabling the deeper decoder to send supervisory signals to the shallower decoder. Finally, by connecting the decoders, a densely connected skip connection is generated so that the dense features propagate along the skip connection, resulting in more flexible feature fusion at the decoder nodes. Thus, each node in the U-Net++ decoder combines multiscale features of the same resolution from all its preceding nodes from a horizontal perspective, and integrates multiscale features of different resolutions from its preceding nodes from a vertical perspective. This multiscale feature aggregation in U-Net++ gradually synthesizes the segmentation, resulting in improved accuracy and fast convergence.

outputs displayed inside a dotted box. At the inference stage, U-Net++ can be pruned by selecting a different output if it was trained with deep supervision.

U-Net++ employs the same encoder for all its substructures, but each substructure has its unique decoder. The central concept of U-Net++ is to bridge the semantic gap between the feature maps of the encoder and decoder before fusing. To achieve this, a dense convolution block with three convolution layers is used to bridge the semantic gap between $(X^{0,0}, X^{1,3})$, for instance.

The proposed technique in this paper aims to accelerate network training by incorporating skip connections. Specifically, by dropping some skip connections and connecting every two neighboring nodes with a short skip connection, the deeper decoder can send supervisory signals to the shallower decoder, leading to faster training. Furthermore, the decoders are connected, creating a densely connected skip connection, which allows dense features to propagate along the skip connection leading to flexible feature fusion. As a result, each node in the U-Net++ decoder combines multi-scale features of the same resolution from all preceding nodes horizontally while integrating multi-scale features of different resolutions from preceding nodes vertically. This multi-scale feature aggregation in U-Net++ gradually synthesizes the segmentation, resulting in improved accuracy and fast convergence.

3.2 Data pre-processing

The U-Net++ model is an evolution of U-Net, sharing many similarities with it. Both models center around semantic segmentation, which detects the class of the object each pixel belongs to for image segmentation (Makinen et al. 2021; Ni et al. 2022). However, it can

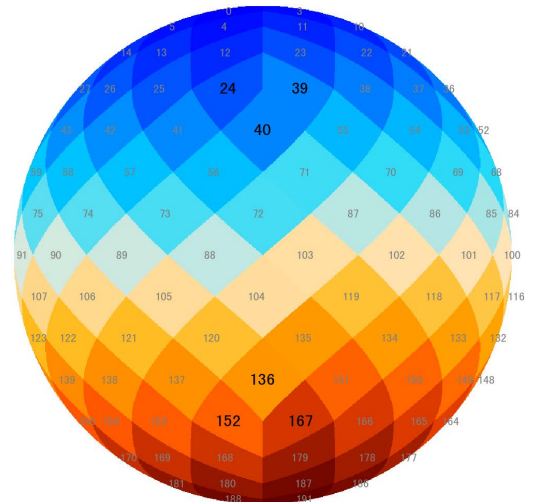


Figure 6. In the case of $N_{side} = 4$, the image presented illustrates a half-orthogonal view projection. In this image, pixels with four neighbors are sequentially labeled in gray, whereas pixels with only three neighbors are highlighted with larger black numbers. It should be noted that only the visible pixels in this view are annotated with their corresponding numbers.

only process 2D flat images or 3D cubes data, not curved images or sky patches directly.

There are currently available network solutions for deep learning on the sphere, such as DeepSphere⁶ (Perraudin et al. 2019) and

⁶ <https://github.com/deepsphere/deepsphere-cosmo-tf1>

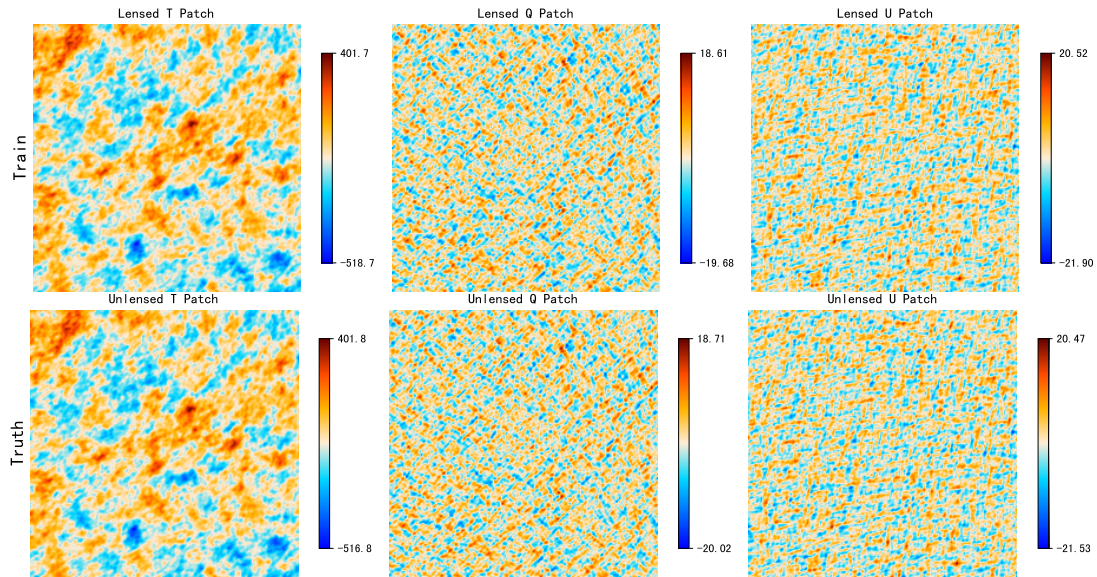


Figure 7. 2D slices from input CMB lensed sky patches (top) and output CMB unlensed sky patches (bottom) for the U-Net++ network. Each patch has a size of 214.86 deg^2 . The center of the sky patches is $(l, b) = (101.25^\circ, 19.47^\circ)$, where l and b are the Galactic longitude and Galactic latitude, respectively. The top row of sky patches is the training dataset, and the bottom row of sky patches is the label. From left to right, the sky patches are T , Q and U map, respectively. The units of the sky patches is mK .

NNhealpix⁷ (Krachmalnicoff & Tomasi 2019). Both methods are highly innovative and have made outstanding contributions to the application of artificial intelligence algorithms on spherical data. We have attempted both methods, but the extremely high resolution of the full sky map we are considering, i.e., $N_{\text{side}} = 2048$, makes both methods extremely time-consuming during the data initialization stage. Furthermore, we have considered that regardless of the segmentation scheme used, as long as the full sky map is not used as training data, boundary processing issues will arise. Therefore, we require more effective methods for data processing and model training to address this issue. Additionally, due to the fact that not all pixels on HEALPix have exactly four neighboring pixels, but in some cases, there are only three, this may also introduce errors in certain segmentation approaches (Krachmalnicoff & Tomasi 2019), as shown in Figure 6.

Our segmentation scheme builds upon Makinen’s work (Makinen et al. 2021). Initially, we approximate each pixel at a resolution of $N_{\text{side}} = 4$ as a flat plane, as shown in Figure 6 with each labeled sky patch. Subsequently, we utilize this as a basis to segment the higher-resolution sky map into patches resembling the $N_{\text{side}} = 4$ sky map. Ultimately, the high-resolution sky map is divided into 192 flat images (corresponding to the number of pixels $N_{\text{side}} = 4$).

The U-Net++ architecture requires square image data with HEALPix pixelization, ensuring equal areas for all images. The full-sky map is divided into small sky patches, consisting of 192 equal-area patches with a pixel area of HEALPix N_{side} of 4. Each patch contains 512×512 pixels. In our data structure, a complete sky map is split into (192, 512, 512), as depicted in Figure 7. The sky patches in the top row constitute the training datasets, while the labels are contained in those at the bottom row.

At any observational scale, cosmology inherently encompasses a wealth of physical information. Assuming that we partition an full sky map into multiple independent regions where there is no scale-

dependent coupling of information among these regions, any form of segmentation will inevitably entail some degree of informational loss, and our segmentation approach is no exception to this principle. Therefore, we have proposed a mitigation strategy to address this issue.

Firstly, the full sky map is subjected to multiple rotation operations aimed at possible directional dependence issues. Subsequently, each rotated image undergoes segmentation processing. Following this, deep learning techniques are employed to conduct meticulous analysis and reconfiguration of the segmented sky patches. Thereafter, the processed sky patches are restored according to their initial rotation angles, and the outcomes obtained from applying the U-Net++ model in multiple iterations are integrated and averaged. Considering our computational resources and time constraints, we have chosen 36 rotation angles. Specifically, longitude = $[-150^\circ, -90^\circ, -30^\circ, 30^\circ, 90^\circ, 150^\circ]$ and latitude = $[-75^\circ, -45^\circ, -15^\circ, 15^\circ, 45^\circ, 75^\circ]$. This methodology effectively reduces the errors introduced by the segmentation scheme, thereby enhancing the preservation and extraction of a more comprehensive set of cosmological information.

This research proposal aims to mitigate the error impact caused by the segmentation operation to a certain degree, but it cannot completely eliminate it. Additionally, the implementation of multiple image rotation processes necessitates the repetition of the corresponding training process, significantly increasing the demands on computational resources and time costs. Consequently, in our experiments, we limited the number of rotation operations to a total of 35 for the training dataset.

Our method exhibits a considerable degree of adaptability and is well-suited for processing full sky map data utilizing the HEALPix segmentation scheme, such as CMB signals, neutral hydrogen full sky temperature and polarization maps, among others. The specific range of applications encompasses the reconstruction of lensing or CMB signals, the removal of neutral hydrogen foregrounds (Makinen et al. 2021), and the elimination of beam (Ni et al. 2022).

⁷ <https://github.com/ai4cmb/NNhealpix>

Table 2. Adjustment and setting of hyperparameters in the U-Net++ architecture design. Prior values indicates that the optimum value is selected from the parameters of the preset value.

Hyperparameter	Description	Prior values	Optimum
η	learning rate	$[10^{-3}, 10^{-4}, 10^{-5}]$	10^{-4}
ω	weight decay	$[10^{-4}, 10^{-5}, 10^{-6}]$	10^{-5}
n_{filters}	filters	[16, 32, 64]	32
b	batch size	[64, 128, 256]	128
Ω	optimizer	[Adam, NAdam]	NAdam

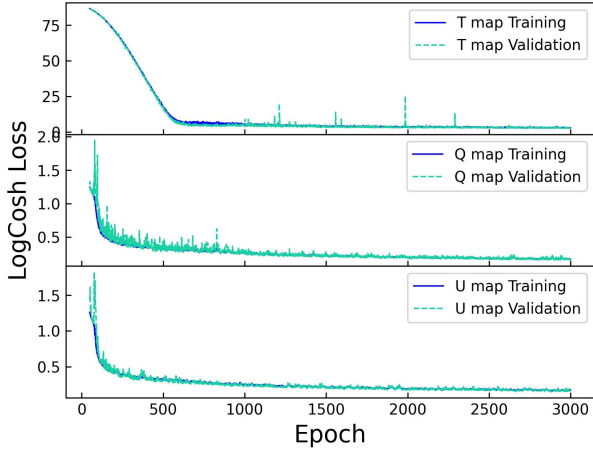


Figure 8. Loss function evolution for each network as a function of the number of epochs. From top to bottom, represent the results of training for T , Q , and U maps, respectively. The dark blue solid line indicates the training set loss function evolution and the light blue dashed line indicates the validation set loss function evolution.

3.3 Loss function

Our goal is to obtain the unlensed CMB from the lensed CMB using a supervised regression algorithm that predicts continuous output values based on input values. Therefore, we analyzed various regression loss functions, including Mean Average Error (MAE, $L1$ norm), Mean Squared Error (MSE, $L2$ norm), Huber, and Log-Cosh. Log-Cosh is a logarithmic hyperbolic cosine loss function that computes the logarithm of the hyperbolic cosine of the prediction error. When the actual value t_i and the predicted value p_i are given, the Log-Cosh function is defined as,

$$L(p, t) = \sum_i \log \cosh(p_i - t_i). \quad (16)$$

The Log-Cosh function exhibits qualities similar to those of the MAE for small losses and MSE for large losses, and features second-order differentiability. In contrast, the Huber loss function is not differentiable in all instances. MAE loss represents the average of absolute errors, and the average absolute distance between the expected and predicted data is incapable of addressing significant errors in predictions. MSE loss is the average of squared errors, and emphasizes significant errors, leading to a relatively large impact on the performance indicator. Consequently, we have chosen the log-cosh function for its superior resistance to outliers.

3.4 Training and testing

U-Net networks are predicated on fully convolutional networks (FCNs), which comprise a convolutional network and an inverse

convolutional network. Thus, the heart of these networks is the convolutional layer, which involves convolving filters on the input data.

In alignment with the works of Makinen et al. and Ni et al. (Makinen et al. 2021; Ni et al. 2022), we have fixed the number of convolutional kernels at the outset of the input to 32. The kernel size determines the convolution’s field of view, which we have established at 3×3 . To achieve the requisite output dimensionality, we have employed “same” padding to manage sample boundaries in both convolutions and transpose convolutions. The stride parameter specifies the kernel’s traversal steps across the image. In our model, we have maintained the default settings of stride = 1 for convolutions and stride = 2 for transpose convolutions.

The U-Net++ architecture was used to train the CMB delensing process via a set of lensed and unlensed CMB sky maps in an end-to-end fashion. Table 2 displays the hyperparameters’ specifics used in this network. The Adam optimizer was utilized in the analysis with the standard TensorFlow parameters (Reddi et al. 2019). The hyperparameters were meticulously fine-tuned for network optimization. The batch size and the initial number of convolutional filters are optimized to 64, 128 and 256, respectively, being restricted by GPU memory. The number of epochs is fixed to 3000; Table 2 illustrates the learning rate setup. Meanwhile, weight decay was examined with a list of previous values listed in Table 2. The optimized values of the initial number of convolution filters, learning rate, weight decay, and batch size were fixed at 32, 10^{-4} , 10^{-5} , 16, respectively. The entire number of trainable parameters is 7.4×10^7 . The total number of trainable parameters is 9.04×10^6 . Since the CMB sky map data contains both positive and negative values due to temperature fluctuations, ReLU and LeakyReLU activation with $\alpha=1.0$ was chosen to handle this relationship. Figure 8 illustrates the evolution of the loss function during the training of T , Q , and U maps as a function of the number of epochs. The figure shows the training results of T , Q , and U maps in a top-to-bottom order. The dark blue line indicates the evolution of the training set loss function, while the light blue dashed line represents the validation dataset’s loss function development.

4 RESULTS AND ANALYSIS

In this section, we conduct a thorough analysis of the results, exploring them in depth from both the sky map and power spectrum perspectives.

4.1 Sky map analysis

Based on the network parameter configuration described in the previous chapter, we have trained multiple datasets and performed prediction operations on the test set. Figure 9 shows the residual performance between the predicted and true values of U-Net++ model processing results. First, in the first row of the figure, we present a small-scale map sample from the test set as a basic reference. Second, in the second row, we show the corresponding small-scale map after delensing processing. Similarly, for comparison and verification, we also provide true small-scale unlensed map data. Finally, in the last row of the figure, to verify the effectiveness of delensing processing, we further show the specific small-scale map of the difference between the predicted and true values.

It can be clearly observed from the analysis of Figure 9 that the delensing method we used has played a significant role in eliminating the lensing effect. To quantitatively evaluate the results, we used two image quality evaluation metrics, namely structural similarity (SSIM) and peak signal-to-noise ratio (PSNR).

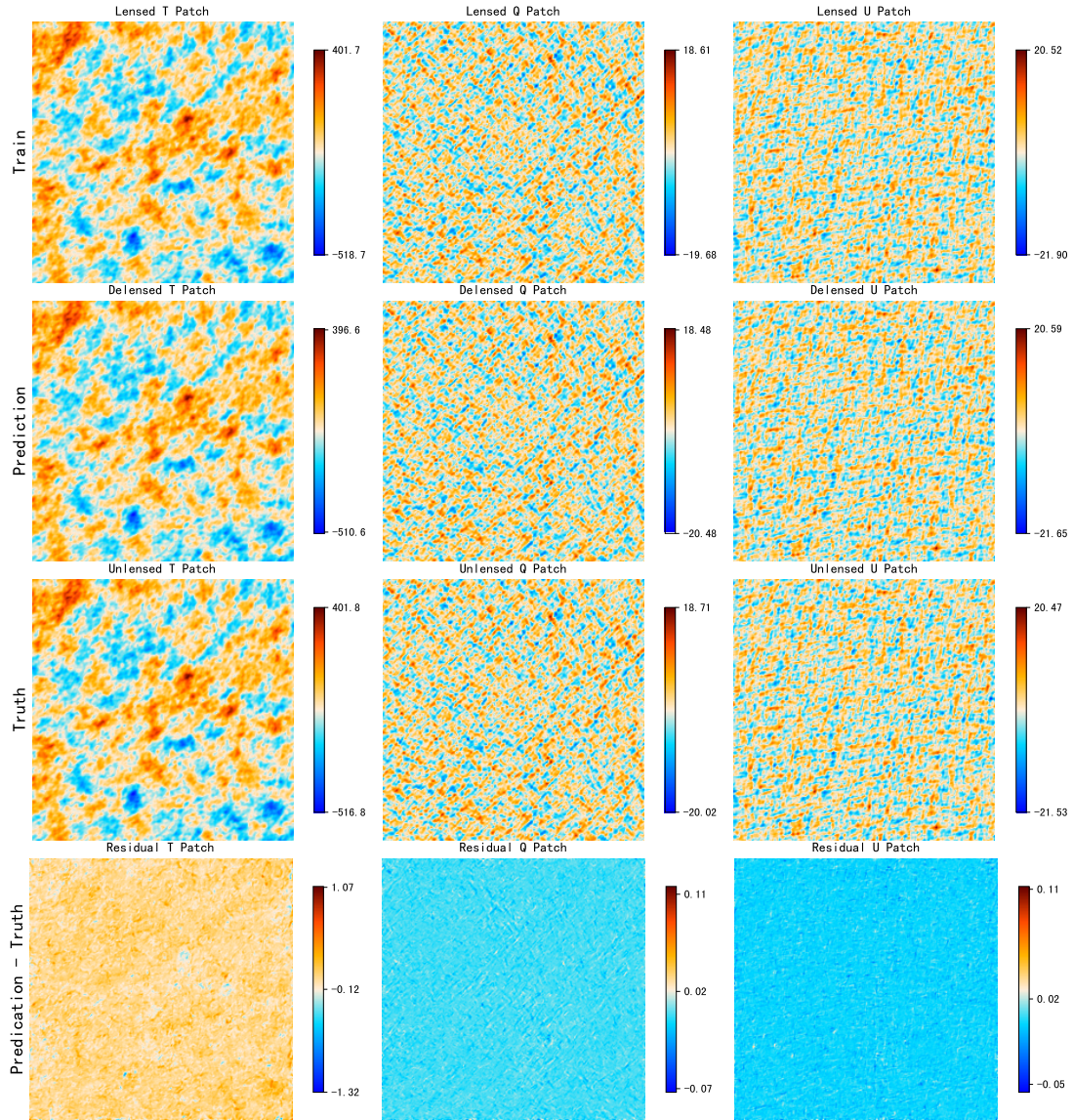


Figure 9. The results of U-Net++ model and the residuals between predictions and true values are displayed. From left to right, the image columns correspond to the samples of sky patches related to T , Q and U fields. From top to bottom: the first row is the test image (lensed sky patches), the second row is the prediction of the test image (delensed sky patches), the third row is the true image (unlensed sky patches), and the last row is the error between the prediction and the true image (residuals between delensed and unlensed). A comparable map schematic can be observed in Figure 7, featuring an image size of 214.86 deg^2 and centered at $(l, b) = (78.75^\circ, 0^\circ)$. The measurement units remains mK .

SSIM is mainly used to analyze the structural information of two images. The closer the SSIM is to 1, the more similar the structural information of the two images is. We have generally processed SSIM by setting the parameters α, β, γ to 1. For the sky patches of two fields \mathcal{F}_1 and \mathcal{F}_2 , we have carried out the following treatment:

$$\begin{aligned} \text{SSIM}(\mathcal{F}_1, \mathcal{F}_2) &= [l(\mathcal{F}_1, \mathcal{F}_2)^\alpha \cdot c(\mathcal{F}_1, \mathcal{F}_2)^\beta \cdot s(\mathcal{F}_1, \mathcal{F}_2)^\gamma] \\ &= \frac{(2\bar{\mathcal{F}}_1\bar{\mathcal{F}}_2 + c_1)[2\text{CoV}(\mathcal{F}_1, \mathcal{F}_2) + c_2]}{(\bar{\mathcal{F}}_1^2 + c_1)[\sigma(\mathcal{F}_1)^2 + \sigma(\mathcal{F}_2)^2 + c_2]}, \end{aligned} \quad (17)$$

where $l(\mathcal{F}_1, \mathcal{F}_2)$, $c(\mathcal{F}_1, \mathcal{F}_2)$, $s(\mathcal{F}_1, \mathcal{F}_2)$ represent the brightness comparison, contrast comparison, and structure comparison between \mathcal{F}_1 and \mathcal{F}_2 , respectively. $\text{CoV}(\mathcal{F}_1, \mathcal{F}_2)$ represents the covariance between \mathcal{F}_1 and \mathcal{F}_2 , while $\sigma(\mathcal{F}_1)$ and $\sigma(\mathcal{F}_2)$ represent the standard deviation

of \mathcal{F}_1 and \mathcal{F}_2 , respectively. c_1 and c_2 are constants to prevent the numerator or denominator from being zero.

We have calculated the structural similarity between the test images (lensed sky patches) and the real images (unlensed sky patches), as well as between the predicted images (delensed sky patches) and the real images, which is shown in Figure 9. The specific results are listed in Table 3. We can see from the table that the SSIM values of delensed T , Q , U sky patches are almost close to 1, indicating that their structures are very similar to those of unlensed sky patches.

As an image quality assessment metric, SSIM fully considers the sensitivity of the human eye to structural information and focuses on differences in image structural information, thus being able to more accurately reflect the quality of the image. However, when comprehensively evaluating image quality, we still need to pay attention to pixel-level errors. Therefore, we further calculate the PSNR value

Table 3. Table of SSIM values between test images (lensed sky patches) and their predicted images (delensed sky patches) and real images (unlensed sky patches) for T , Q , and U .

SSIM($\mathcal{F}_1, \mathcal{F}_2$)		(T, T)	(Q, Q)	(U, U)
Images($1, 2$)				
	(train, truth)	0.7542	0.7065	0.7141
	(pred, truth)	0.9952	0.9933	0.9942

Table 4. Table of PSNR values between test images (lensed sky patches) and their predicted images (delensed sky patches) and real images (unlensed sky patches) for T , Q , and U .

PSNR($\mathcal{F}_1, \mathcal{F}_2$)		(T, T)	(Q, Q)	(U, U)
Images($1, 2$)				
	(train, truth)	33.01	26.54	26.87
	(pred, truth)	46.96	45.69	46.30

between different images, using the following specific formula:

$$PSNR(\mathcal{F}_1 - \mathcal{F}_2) = 10 \cdot \log_{10} \left[\frac{\text{MAX}(\mathcal{F}_1, \mathcal{F}_2)}{\text{MSE}(\mathcal{F}_1, \mathcal{F}_2)} \right] \text{dB}, \quad (18)$$

where $\text{MAX}(\mathcal{F}_1, \mathcal{F}_2)$ represents the maximum pixel difference between images \mathcal{F}_1 and \mathcal{F}_2 , and $\text{MSE}(\mathcal{F}_1, \mathcal{F}_2)$ represents the mean squared error between \mathcal{F}_1 and \mathcal{F}_2 . Through this calculation, we can more comprehensively evaluate the degree of distortion at the pixel level in the image, and thus provide strong support for the comprehensive evaluation of image quality.

PSNR stands as a simple yet widely utilized metric for assessing image quality, employing the decibel (dB) as its unit of measurement. Within this evaluative framework, a higher numerical value signifies a lower degree of image distortion, thereby indicating superior image quality. Akin to the computation of the SSIM metric, we have also conducted a corresponding analytical calculation of the PSNR, as shown in Table 4.

PSNR measures the degree of image distortion by calculating the pixel differences between images. According to the results presented in Table 4, we can clearly observe that the delensed sky patches, compared to the original lensed sky patches, exhibit a significant advantage in terms of the PSNR metric, with notably higher values. This indicates that the delensed sky patches are superior in preserving details and conveying information, effectively reducing the degree of image distortion.

Although SSIM and PSNR highly affirm the accuracy of the predicted data in numerical terms, they only quantitatively compare the pixel values of the test data with the truth data, without considering whether the predicted images have the same physical meaning or research value as the real images. Therefore, we need to conduct in-depth research on the angular power spectrum of delensed CMB maps.

4.2 Angular power spectrum analysis

In this subsection of the study, we conducted a comprehensive analysis of the angular power spectrum of the CMB temperature and polarization. Following multiple iterations of U-Net++ network training, we present the power spectra of CMB TT , BB , EE , and TE , as illustrated in Figures 10-13. The upper portion of the figures depicts the power spectra, with red indicating lensed, blue denoting unlensed, and orange representing delensed. The lower section illustrates the ratios between lensed, unlensed, and delensed components. Specifically, the pink color corresponds to $C_\ell^{\text{delensed}}/C_\ell^{\text{lensed}}$, the light

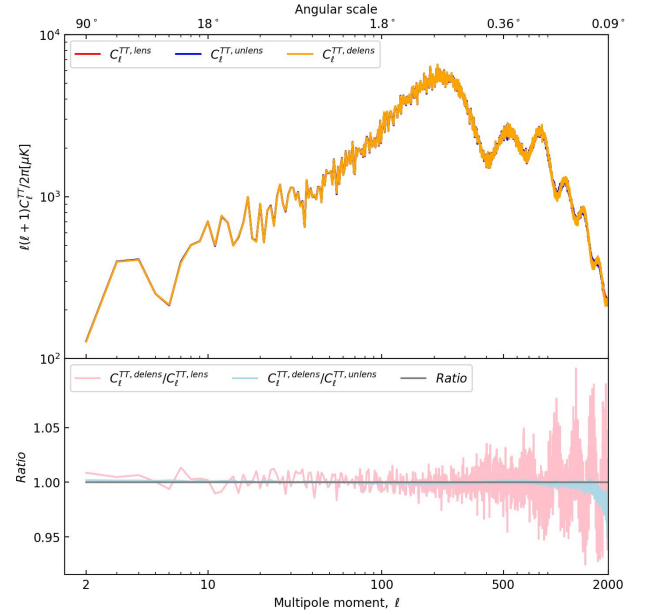


Figure 10. The lensed, unlensed, and delensed CMB TT power spectrum, along with their respective ratios. *Top panel:* The red solid line represents the lensed TT spectrum, the blue solid line represents the unlensed TT spectrum, and the orange solid line represents the delensed TT spectrum; *Bottom panel:* The pink solid line represents the ratio between the delensed TT spectrum and lensed lensed spectrum, the light blue solid line represents the ratio between the unlensed TT spectrum and the lensed TT spectrum, and the gray solid line represents Ratio = 1.

blue color signifies $C_\ell^{\text{delensed}}/C_\ell^{\text{unlensed}}$, and the gray color denotes Ratio = 1.

In order to more intuitively compare the effects of delensing on various scales, we introduce two quantities to quantify the results of this process, which are specifically defined as follows:

$$\Gamma^{XX, \text{lensed}} = \text{Mean} \left(\left| \frac{C_\ell^{XX, \text{lensed}}}{C_\ell^{XX, \text{unlensed}}} - 1 \right| \right), \quad (19)$$

$$\Gamma^{XX, \text{delensed}} = \text{Mean} \left(\left| \frac{C_\ell^{XX, \text{delensed}}}{C_\ell^{XX, \text{unlensed}}} - 1 \right| \right),$$

where the subscript $XX = \{TT, EE, BB, TE\}$. The subscript *lensed* corresponds to the quantized CMB lensed power spectrum, while the subscript *delensed* represents the quantized CMB delensed power spectrum. The term Mean specifically refers to the calculation of the average value of an array that is enclosed within parentheses. The physical interpretation of Equation (19) is that a value of Γ^{XX} approaching zero indicates a diminished impact of the lensing effect.

We initiate our investigation with an in-depth analysis of Figure 10, which illustrates the lensed, unlensed, and delensed CMB TT angular power spectrum, as well as their corresponding ratios. Upon careful examination of the image, we observed that the delensed and unlensed angular power spectra are highly similar on larger scales (smaller ℓ values). Based on the quantitative index for calculation [Equation (19)], we obtained the results of $\Gamma^{TT, \text{lensed}} = 0.0194$ and $\Gamma^{TT, \text{delensed}} = 0.0023$, which indicate the significant impact of the delensing treatment.

However, as we focus on smaller scales (corresponding to an increase in ℓ), the difference between the delensed and unlensed power spectra gradually increases, with the delensed spectrum showing a decreasing trend. This phenomenon reveals the varying performance

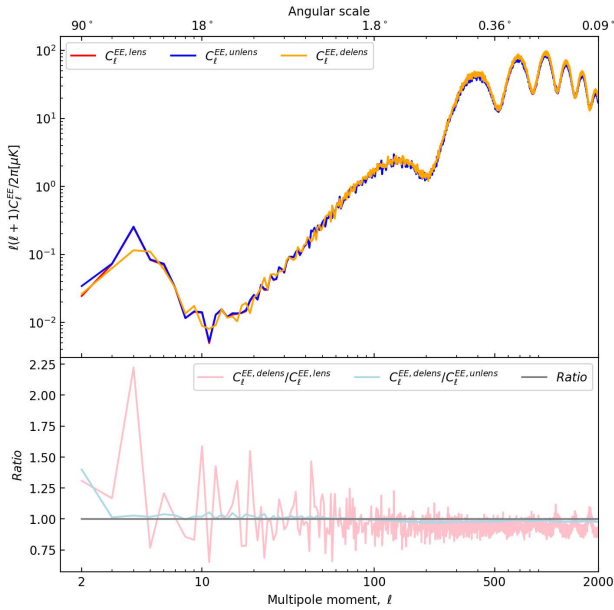


Figure 11. The lensed, unlensed, and delensed CMB EE power spectrum, along with their respective ratios. *Top panel:* The red solid line represents the lensed EE spectrum, the blue solid line represents the unlensed EE spectrum, and the orange solid line represents the delensed EE spectrum. *Bottom panel:* The pink solid line represents the ratio between the delensed EE spectrum and lensed spectrum, the light blue solid line represents the ratio between the delensed EE spectrum and the unlensed EE spectrum, and the gray solid line represents Ratio = 1.

of the U-Net++ network across different scales. Specifically, as the scale decreases, the delensing effect of U-Net++ diminishes gradually, and the rate of this decrease accelerates. We propose two possible explanations for this finding.

Firstly, we believe that the lensing effect may gradually increase on smaller scales, causing a significant distortion of the original CMB signal. This distortion may exceed the correction capability of the U-Net++ network, leading to a decrease in delensing effectiveness on even smaller scales. Secondly, we considered the impact of the segmentation scheme selection on the results. In this study, we used $N_{side} = 4$ as the base resolution for segmentation, which may have adverse effects on the delensing effectiveness on smaller scales.

To investigate the validity of the second hypothesis, we conducted further calculations and analyses. When $N_{side} = 4$, each pixel covers approximately 214.86 square degrees on the sky, corresponding to a multipole moment ℓ of around 100. However, Figure 1 shows significant anomalies only when ℓ is greater than 1000. Hence, we can initially dismiss the segmentation scheme as the primary reason for the decreased delensing effectiveness on smaller scales. Consequently, the most probable reason for the decreased delensed effect of U-Net++ on smaller scales is the first explanation: U-Net++ cannot effectively remove the lensing effect when the lensing effect is substantial.

Figure 11 illustrates the lensed, unlensed and delensed CMB EE angular power spectra, along with their corresponding ratios. Through detailed analysis of the image, we find that the differences among these three power spectra are not significant. Nevertheless, in the ratio plot, a conspicuous oscillation emerges in the power spectrum of the large scale (small ℓ values), which are primarily caused by cosmic variance, but have no impact on our research results.

To more specifically evaluate the effectiveness of the delensing effect, we also calculated quantitative indicators using Equation (19),

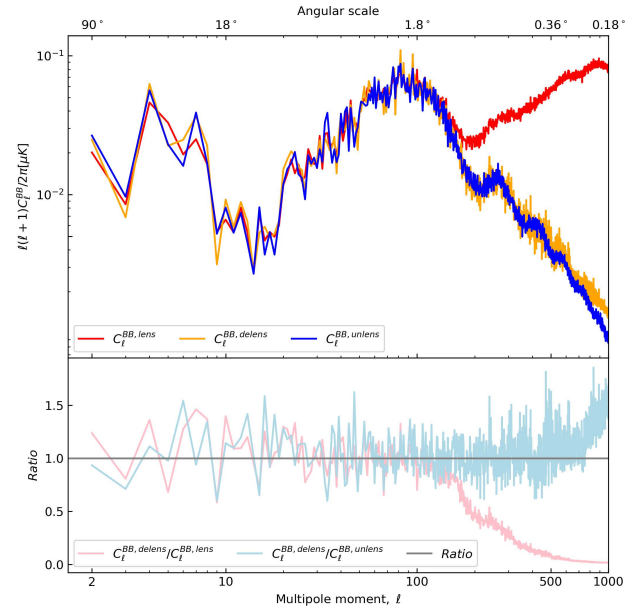


Figure 12. The lensed, unlensed, and delensed CMB BB power spectrum, along with their respective ratios. *Top panel:* The red solid line represents the lensed BB spectrum, the blue solid line represents the unlensed BB spectrum, and the orange solid line represents the delensed BB spectrum. *Bottom panel:* The pink solid line represents the ratio between the delensed BB spectrum and lensed spectrum, the light blue solid line represents the ratio between the delensed BB spectrum and the unlensed BB spectrum, and the gray solid line represents Ratio = 1.

obtaining $\Gamma^{EE, lensed} = 0.0687$ and $\Gamma^{EE, delensed} = 0.0276$. These two values indicate that the EE spectrum has seen a notable improvement after undergoing the delensing treatment, and that the delensing capabilities of the TT and EE spectra are roughly equivalent.

Similar to the case of the TT spectrum, as we focus on the EE spectrum at smaller scales, the difference between the delensed spectrum and the lensed spectrum gradually increases. This is also due to the inherent limitations of the U-Net++ model in terms of its delensing capabilities.

Figure 12 presents the lensed, unlensed, and delensed BB angular power spectra of the CMB, along with their corresponding ratios. Notably, compared to the TT and EE spectra, the lensing potential has a particularly significant impact on the BB spectrum. There are three main reasons for this phenomenon. Firstly, the lensing potential not only converts E -mode signals into B -mode signals, but also reverses the process, converting B -mode signals back into E -mode signals. This may lead to hallucination effects in the U-Net++ network. Secondly, the unlensed B -mode signal itself is extremely weak, even below the level of the conversion signal from E -mode to B -mode caused by the lensing effect. Therefore, under the influence of the lensing effect, the difference between the lensed BB spectrum and the unlensed BB spectrum becomes particularly prominent. This difference is visually reflected in Figure 2, demonstrating the order of magnitude difference in the impact of the lensing effect on the BB spectrum. Finally, the difference between lensed BB and unlensed BB is extremely significant at small scales, approaching 10^4 . The processing of such High-Dynamic-Range data may be limited in terms of the effectiveness and generalization capabilities of deep learning.

Upon further examination of Figure 12, it can be observed that U-Net++ performs well in delensing on large scales. However, as the scale decreases, its effectiveness gradually diminishes. While this is partly due to the inherent limitations of U-Net++ in delensing, the

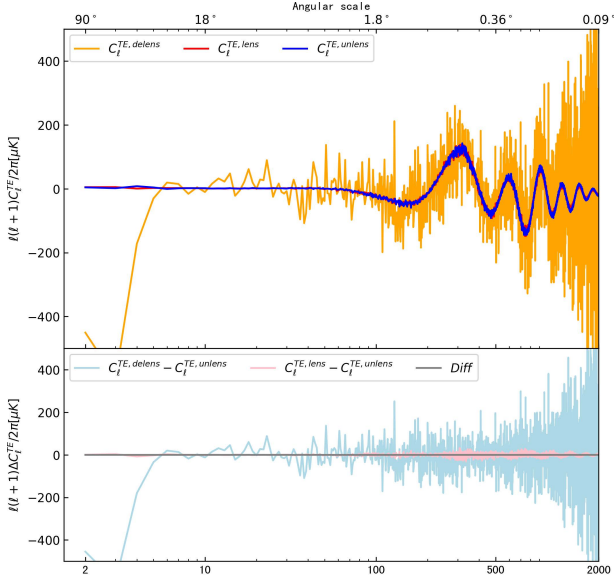


Figure 13. The lensed, unlensed, and delensed CMB TE power spectrum, along with their respective ratios. *Top panel:* The orange solid line represents the delensed TE spectrum; the red solid line represents the lensed TE spectrum; the blue solid line represents the unlensed TE spectrum. *Bottom panel:* The light blue solid line demonstrates the differences between the delensed TE spectrum and the unlensed TE spectrum; the pink solid line portrays the differences between the lensed TE spectrum and the unlensed TE spectrum. As a reference benchmark, the grey solid line labeled $\text{Diff} = 0$ represents a state of perfect consistency where there is no difference between the two spectra.

primary reason lies in the strong influence of the lensing potential on the BB spectrum. This also highlights the deficiency of the generalization ability of deep learning under the U-Net network structure for High-Dynamic-Range data (Makinen et al. 2021; Ni et al. 2022). To quantify this influence, we adopted a similar approach as used for the TT and EE spectra and calculated relevant metrics using Equation (19), namely $\Gamma^{BB, \text{lensed}} = 2475.83$, $\Gamma^{BB, \text{delensed}} = 0.5138$. The results indicate that U-Net++ can effectively perform delensing on large scales; however, on small scales, especially when the multipole moment (l) is greater than 500, the effectiveness of delensing is almost completely lost. To more intuitively demonstrate these quantitative results, we also performed segmented calculations using Equation (19) for the ranges $2 < l < 500$ and $500 < l < 1000$. The respective results of $\Gamma_{2 < l < 500}^{BB, \text{lensed}} = 332.46$, $\Gamma_{500 < l < 1000}^{BB, \text{delensed}} = 0.3163$ and $\Gamma_{2 < l < 500}^{BB, \text{lensed}} = 4614.94$, $\Gamma_{500 < l < 1000}^{BB, \text{delensed}} = 0.7110$ further confirm the significant decrease in the effectiveness of U-Net++’s delensing capabilities on small scales.

Figure 13 presents the CMB TE angular power spectra of lensed, unlensed, and delensed cases. Given the characteristics of the TE spectrum, we used the difference in lensing effects as the comparison benchmark. Unlike the auto-correlation power spectra such as TT , EE , and BB , the TE spectrum is a cross-correlation power spectrum that reflects the correlation between the CMB T -mode and E -mode at different scales. From the upper panel of Figure 3, we can clearly observe the anti-peak and peak of the lensed and unlensed C_l^{TE} .

In the top panel of Figure 13, both the training data (lensed, unlensed) and the prediction data (delensed) exhibit non-zero correlation. Notably, the delensed data also exhibits distinct anti-peak and peak, confirming that our network did not resort to brute-force methods to solve the delensing process but truly learned the underlying

differences between lensed and unlensed sky map. However, in the bottom panel of Figure 13, we also notice that the noise level of the prediction data is significantly higher compared to the real data (unlensed), especially at smaller scales. This may be due to the limited utilization of global contextual information by U-Net++, which primarily relies on local information for pixel-level predictions.

5 CONCLUSIONS

The continuous advancements in deep learning technology have significantly bolstered its application in cosmological research. These studies not only validate the potential of neural networks as an alternative to traditional methods for correcting CMB lensing effects, but also drive further innovation within the domain. We draw upon this series of research findings and adopt the advanced U-Net++ network architecture to perform refined delensing processing on CMB images, which can accurately identify and extract feature information at the pixel level. This study integrates the sky map segmentation technique, as suggested by researchers like Makinen et al. (2021), into CMB delensing methods for the first time, aimed at overcoming the challenges posed by weak gravitational lensing effects.

In large-scale observations of the CMB, subtle cosmological signals, particularly B -mode polarization signals, are extremely weak and easily contaminated by foreground emissions. Moreover, the inevitable weak gravitational lensing phenomenon distorts the original CMB image during the cosmic evolution, causing mixing conversions between T modes and E modes, as well as between E modes and B modes. Therefore, finding effective means to remove the interference from weak gravitational lensing on CMB data is one of the key challenges in revealing the genuine B -mode polarization signal.

In this work, we employ a novel full sky map segmentation scheme (Makinen et al. 2021; Ni et al. 2022; Gao et al. 2023). While DeepSphere and NNhealpix have made significant advancements in processing full sky MB images, they often require excessively long initialization times, surpassing even model training times when dealing with high-resolution datasets ($N_{\text{side}} = 2048$). In contrast, our method significantly optimizes this process, ensuring initialization time remains under second-level standard while maintaining efficient training speed. Additionally, to enhance the realism of our simulations resembling actual astronomical observations, we include instrumental noise and effects in our analysis. The primary focus of this research is to investigate whether deep learning methods, particularly the U-Net++ algorithm, can play a pivotal role in tackling the challenge of removing weak gravitational lensing effects from CMB data.

In the delensing study of full sky map for CMB temperature T , polarization Q and U components, the U-Net++ network demonstrates remarkable performance. Evaluating image quality metrics, we find that both SSIM and PSNR show significant improvements. Specifically, when processing T maps, SSIM and PSNR improve by 31.95% and 42.46%, respectively, while for Q and U maps, these indices see even more pronounced improvements, increasing approximately by 42% and up to 72%, strongly indicating that the U-Net++ network can effectively remove gravitational lensing effects at the pixel level.

At the power spectrum level, we examined the characteristic changes in the TT , EE , BB , and TE spectra. By calculating the quantification function we set, we found that on the delensed TT spectrum, the $\Gamma^{TT, \text{delensed}}$ value was only 0.0023, significantly lower than the $\Gamma^{TT, \text{lensed}}$ value of 0.0194 before delensing, indicating a pronounced delensing effect. Similarly, significant improvements were observed in the EE spectrum, with $\Gamma^{EE, \text{delensed}} = 0.0276$

and $\Gamma^{EE, \text{lensed}} = 0.0687$. Due to the significant differences between the lensed and unlensed BB spectra, the BB delensing effect was even more pronounced, with $\Gamma^{BB, \text{delensed}} = 0.5137$ across all scales, compared to $\Gamma^{BB, \text{lensed}} = 2473.70$. Although the BB spectrum had already shown notable improvement from its initial state, potential for further enhancement in the delensing effect at smaller scales remained evident. As for the TE spectrum, although the delensing results were significantly affected by noise, the anti-peak and peak features presented in the predicted images suggested that the U-Net++ network had successfully learned the pattern differences between lensed and unlensed spectra and possessed a certain degree of generalization ability. This ruled out the possibility that the model had simply used a brute-force method to fit the delensing results. This implies that the U-Net++ network can understand and effectively simulate the physical process from lensing to delensing.

While the U-Net++ model achieves remarkable results in CMB delensing tasks, we note a decreasing trend in the recovery effect for all components in the small-scale power spectra. Although initially speculated to be due to limitations of the segmentation scheme at extremely high resolutions and small scales, after in-depth exploration of resolution and feature scales, we exclude this possibility.

Based on current analyses, we infer that the U-Net mainly relies on local information for pixel-level predictions, with limited utilization of global context information. For scenarios requiring more accurate segmentation with global context information, additional designs such as self-attention mechanisms or other forms of global pooling operations might be needed to enhance model performance. Consequently, in future work, we will attempt to improve this method by incorporating attention mechanisms, multi-scale fusion, deeper and wider network structure designs, and specific data augmentation strategies.

Looking ahead, our primary focus will be on the delensing of CMB B -mode polarization sky maps. This is because the impact of weak gravitational lensing on CMB B modes is significantly greater compared to T modes and E modes. CMB B -mode polarization sky map's delensing is a crucial task for detecting primordial gravitational waves and understanding inflationary cosmology. Thus, gravitational lensing effects may potentially mask critical signals of interest, rendering the detection of primordial gravitational waves from cosmic inflation unattainable.

ACKNOWLEDGMENTS

We thank Sebastian Belkner for his valuable suggestions and guidance on the correct use of lenspyx. This work was supported by the National SKA Program of China (Grants Nos. 2022SKA0110200 and 2022SKA0110203), the National Natural Science Foundation of China (Grants Nos. 11975072, 11835009, and 11875102), the Liaoning Revitalization Talents Program (Grant No. XLYC1905011), the National 111 Project of China (Grant No. B16009), and the Science Research Grants from the China Manned Space Project (Grant No. CMS-CSST-2021-B01).

DATA AVAILABILITY

The data underlying this article will be shared on reasonable request to the corresponding author.

REFERENCES

- Abazajian K. N., et al., 2016
 Abazajian K., et al., 2022
 Aboobaker A. M., et al., 2018, *Astrophys. J. Suppl.*, 239, 7
 Ade P. A. R., et al., 2014a, *Phys. Rev. Lett.*, 112, 241101
 Ade P. A. R., et al., 2014b, *Astron. Astrophys.*, 571, A16
 Ade P. A. R., et al., 2014c, *Astrophys. J.*, 792, 62
 Ade P. A. R., et al., 2015, *Phys. Rev. Lett.*, 114, 101301
 Ade P. A. R., et al., 2016, *Astron. Astrophys.*, 594, A13
 Ade P., et al., 2019, *JCAP*, 02, 056
 Aghanim N., et al., 2020, *Astron. Astrophys.*, 641, A6
 Akrami Y., et al., 2020, *Astron. Astrophys.*, 641, A2
 Allys E., et al., 2023, *PTEP*, 2023, 042F01
 Barkats D., et al., 2014, *Astrophys. J.*, 783, 67
 Bartelmann M., Schneider P., 2001, *Phys. Rept.*, 340, 291
 Baumann D., 2011, in *Theoretical Advanced Study Institute in Elementary Particle Physics: Physics of the Large and the Small*. pp 523–686 ([arXiv:0907.5424](https://arxiv.org/abs/0907.5424)), doi:10.1142/9789814327183_0010
 Bennett C. L., et al., 1996, *Astrophys. J. Lett.*, 464, L1
 Bunn E. F., Zaldarriaga M., Tegmark M., de Oliveira-Costa A., 2003, *Phys. Rev. D*, 67, 023501
 Caldeira J. a., Wu W. L. K., Nord B., Avestruz C., Trivedi S., Story K. T., 2019, *Astron. Comput.*, 28, 100307
 Carlstrom J. E., et al., 2011, *Publ. Astron. Soc. Pac.*, 123, 568
 Coulton W., et al., 2023
 Crill B. P., et al., 2008, *Proc. SPIE Int. Soc. Opt. Eng.*, 7010, 70102P
 Di Dio E., Montanari F., Lesgourgues J., Durrer R., 2013, *JCAP*, 11, 044
 Diego-Palazuelos P., Vielva P., Martínez-González E., Barreiro R. B., 2020, *JCAP*, 11, 058
 Dodelson S., Schmidt F., 2021, *Probes of structure: lensing*. pp 373–399, doi:10.1016/B978-0-12-815948-4.00019-X
 Fixsen D. J., Cheng E. S., Gales J. M., Mather J. C., Shafer R. A., Wright E. L., 1996, *Astrophys. J.*, 473, 576
 Gao L.-Y., Li Y., Ni S., Zhang X., 2023, *Mon. Not. Roy. Astron. Soc.*, 525, 5278
 Ghosh S., Das I., Das N., Maulik U., 2019, *ACM Computing Surveys*, 52, 40
 Górski K. M., Hivon E., Banday A. J., Wandelt B. D., Hansen F. K., Reinecke M., Bartelman M., 2005, *Astrophys. J.*, 622, 759
 Gupta A., Matilla J. M. Z., Hsu D., Haiman Z., 2018, *Phys. Rev. D*, 97, 103515
 Guzman E., Meyers J., 2022, *JCAP*, 01, 030
 Hanany S., et al., 2019
 Hassani F., Baghran S., Firouzjahi H., 2016, *JCAP*, 05, 044
 Hu W., 2000, *Phys. Rev. D*, 62, 043007
 Kamionkowski M., Kovetz E. D., 2016, *Ann. Rev. Astron. Astrophys.*, 54, 227
 Kamionkowski M., Kosowsky A., Stebbins A., 1997a, *Phys. Rev. D*, 55, 7368
 Kamionkowski M., Kosowsky A., Stebbins A., 1997b, *Phys. Rev. Lett.*, 78, 2058
 Kim J., Naselsky P., 2010, <http://dx.doi.org/10.1051/0004-6361/201014739>, 519
 Komatsu E., et al., 2009, *Astrophys. J. Suppl.*, 180, 330
 Komatsu E., et al., 2011, *Astrophys. J. Suppl.*, 192, 18
 Krachmalnicoff N., Tomasi M., 2019, *Astron. Astrophys.*, 628, A129
 Lazear J., et al., 2014, *Proc. SPIE Int. Soc. Opt. Eng.*, 9153, 91531L
 Leitch E. M., et al., 2002, *Nature*, 420, 763
 Lewis A., 2005, *Phys. Rev. D*, 71, 083008
 Lewis A., 2013, *Phys. Rev. D*, 87, 103529
 Lewis A., Challinor A., 2006, *Phys. Rept.*, 429, 1
 Lewis A., Challinor A., Lasenby A., 2000, *Astrophys. J.*, 538, 473
 Li H., et al., 2019, *Natl. Sci. Rev.*, 6, 145
 Lucca M., Schöneberg N., Hooper D. C., Lesgourgues J., Chluba J., 2020, *JCAP*, 02, 026
 Lyth D. H., Riotto A., 1999, *Phys. Rept.*, 314, 1
 Mäkinen T. L., Lancaster L., Villaescusa-Navarro F., Melchior P., Ho S., Perreault-Levasseur L., Spergel D. N., 2021, *JCAP*, 04, 081
 Masi S., et al., 2002, *Prog. Part. Nucl. Phys.*, 48, 243

- Minaee S., Boykov Y., Porikli F., Plaza A., Kehtarnavaz N., Terzopoulos D., 2021, [IEEE transactions on pattern analysis and machine intelligence](#), PP
- Ni S., Li Y., Gao L.-Y., Zhang X., 2022, [Astrophys. J.](#), 934, 83
- Okamoto T., Hu W., 2003, [Phys. Rev. D](#), 67, 083002
- Perraudin N., Defferrard M., Kacprzak T., Sgier R., 2019, [Astron. Comput.](#), 27, 130
- Readhead A. C. S., et al., 2004, [Science](#), 306, 836
- Reddi S. J., Kale S., Kumar S., 2019
- Ronneberger O., Fischer P., Brox T., 2015. pp 234–241, [doi:10.1007/978-3-319-24574-4_28](#)
- Rotti A., Huffenberger K., 2019, [JCAP](#), 01, 045
- Smoot G. F., et al., 1992, [Astrophys. J. Lett.](#), 396, L1
- Spergel D. N., et al., 2003, [Astrophys. J. Suppl.](#), 148, 175
- Springer O. M., Ofek E. O., Weiss Y., Merten J., 2020, [Mon. Not. Roy. Astron. Soc.](#), 491, 5301
- Staniszewski Z., et al., 2012, [J. Low Temp. Phys.](#), 167, 827
- Wang G., et al., 2018, [IEEE Transactions on Medical Imaging](#), 37, 1562
- Wolz K., et al., 2023
- Wu W. L. K., Errard J., Dvorkin C., Kuo C. L., Lee A. T., McDonald P., Slosar A., Zahn O., 2014, [Astrophys. J.](#), 788, 138
- Wu D., Li H., Ni S., Li Z.-W., Liu C.-Z., 2020, [The European Physical Journal C](#), 80
- Zaldarriaga M., 1998, [The Astrophysical Journal](#), 503, 1
- Zaldarriaga M., Seljak U., 1997, [Phys. Rev. D](#), 55, 1830
- Zaldarriaga M., Seljak U., 1998, [Phys. Rev. D](#), 58, 023003
- Zhang X., Wang Y., Zhang W., Sun Y., He S., Contardo G., Villaescusa-Navarro F., Ho S., 2019
- Zhou Z., Siddiquee M. M. R., Tajbakhsh N., Liang J., 2018, [CoRR](#), abs/1807.10165
- Zhou Z., Siddiquee M. M. R., Tajbakhsh N., Liang J., 2019, [IEEE Transactions on Medical Imaging](#), 39, 1856
- Zonca A., Singer L., Lenz D., Reinecke M., Rosset C., Hivon E., Gorski K., 2019, [Journal of Open Source Software](#), 4, 1298

This paper has been typeset from a $\text{\TeX}/\text{\LaTeX}$ file prepared by the author.